Influence of casting defect and SDAS on the multiaxial fatigue behaviour of A356-T6 alloy including mean stress effect

Mohamed Iben Houria, Yves Nadot, Raouf Fathallah, Matthew Roy, Daan Maijer

Influence of casting defect and SDAS on the multiaxial fatigue behaviour of A356-T6 alloy including mean stress effect

Mohamed Iben Houria [a,b,*], Yves Nadot [a,1], Raouf Fathallah [b,2], Matthew Roy [c,3], Daan M. Maijer [d,4]

a PPRIME institute, ISAE-ENSMA, UPR CNRS 3346, Material Engineering Department, 1 Avenue Clément Ader, Téléport 2 – BP 40109, F86961 FUTUROSCOPE CHASSENEUIL Cedex, France
b Laboratoire de Mécanique de Sousse, Ecole Nationale d'Ingénieurs de Sousse, Bp 264 erriadh, 4023 Sousse, Tunisia
c School of Mechanical, Aerospace and Civil Engineering, The University of Manchester, B38g Sackville St. Building, Manchester M13 9PL, UK
d Dept. of Materials Engineering, University of British Columbia, Vancouver, BC V6T 1Z4, Canada

The effect of mean stress on the multiaxial High Cycle Fatigue (HCF) behaviour of cast A356-T6 alloy containing natural and artificial defects with varying Secondary Dendrite Arming Spacing (SDAS) has been investigated experimentally. Tension, torsion and combined tension–torsion fatigue tests have been performed for two loading ratios: $R_\sigma = 0$ and $R_\sigma = -1$. A Scanning Electron Microscopy (SEM) was used to perform fractographic analysis of the fracture surfaces to characterise the defect causing failure. In order to gauge the effect of mean stress and defects, the results are reported with standard Kitagawa and Haigh diagrams. A surface response method has been employed to characterise the influence of defect size and SDAS on the fatigue limit. Relationships and correlations describing the observed behaviour have been incorporated in the Defect Stress Gradient (DSG) criterion with the goal of determining the influence of defects on the fatigue limit through a stress gradient approach.

Results clearly show that: (i) the mean stress has a detrimental effect on the fatigue limit. This effect is a function of the loading, which is most pronounced under tension, less under combined tension–torsion, and least pronounced under torsion conditions; (ii) in the absence of defects, the SDAS controls the fatigue limit of cast A356, this effect is much more important under torsion loading; (iii) the DSG criterion is improved by the mean of a parameter describing the microstructure effect through the SDAS.

1. Introduction

Cast aluminum components are employed in a large number of automotive and aerospace applications as they are lightweight, corrosion resistant and relatively inexpensive. A356 is a common aluminum foundry alloy that provides a good balance between optimal casting properties and post heat treatment mechanical strength, with components typically receiving a T6 treatment prior to service. However, cast materials often contain defects owing to a variety of causes such as difficulties in controlling solidification parameters, metal quality and casting procedures. The two defects that are the most difficult to eliminate are gas and shrinkage porosity. The present work will focus on the fatigue resilience of low-pressure die cast A356 in the T6 condition and the influence of these two different defect types.

The fatigue behaviour of cast materials with pre-existing defects is a function of crack initiation and propagation close proximity to the defects. A number of experimental investigations have been carried out for the A356-T6 material [1–6]. It has been clearly observed that the fatigue behaviour of the A356 aluminum alloy is dominated by the presence of defects. As reported in [5], in the absence of casting defects, the influence of the microstructure measured by the Dendrite Arm Spacing DAS or SDAS, on the fatigue behaviour cannot be neglected. Gao et al. [7] showed that the fatigue resistance of A356-T6 is strongly dependent on the microstructure and defects in cast aluminum alloys. In this case, the eutectic phase have a significant role in micro-crack initiation for defect free material. It was demonstrated that micro-plastic strain accumulation in proximity to the Si-particles in the eutectic phase, induces micro-crack initiation.

* Corresponding author. Tel.: +33 6 63 02 46 16.
E-mail addresses: mohamed.iben-houria@ensma.fr (M. Iben Houria), yves.nadot@ensma.fr (Y. Nadot), raouf.fathallah@gmail.com (R. Fathallah), matthew.roy@manchester.ac.uk (M. Roy), daan.maijer@ubc.ca (D.M. Maijer).
[1] Tel.: +33 5 49 49 80 43.
[2] Tel.: +216 98 22 88 69; fax: +216 73 369 506.
[3] Tel.: +44 (0)747 254 9932.
[4] Tel.: +1 604 822 6013; fax: +1 604 822 3619.

Nomenclature

a_∇	material parameter describing the type of defect and its influence in the DSG approach (μm)
n	Basquin coefficient
A	material elongation (%)
D	distance between two defects (μm)
D_{max}	maximum distance between two defects (μm)
E	Young modulus (GPa)
N	number of cycles
N_f	number of cycles to failure
R_m	tensile strength (MPa)
$R_{p0.2}$	yield stress at 0.2% plastic deformation (MPa)
R_σ	load ratio between over the loading cycle $R_\sigma = \sigma_{min}/\sigma_{max}$
α_{cr}	material parameter in the Crossland criterion
β_{cr}	material parameter in the Crossland criterion (MPa)
λ_2	secondary dendrite arming spacing (μm)
ε	error in the response surface method
σ_a	stress amplitude (MPa)
σ_{Cr}	Crossland equivalent stress (MPa)
σ_D	fatigue limit equal to the stress amplitude corresponding to 10^6 cycles (MPa)
σ_{max}	maximum stress (MPa)
σ_{min}	minimum stress (MPa)
σ_{mean}	mean stress (MPa)
σ_y	yield stress (MPa)
σ_{D-1}^{to}	fatigue limit under fully reversed torsion ($R_\sigma = -1$) (MPa)
σ_{D-1}^{te}	fatigue limit under fully reversed tension ($R_\sigma = -1$) (MPa)
σ_{D-1}^{te-to}	fatigue limit under fully reversed tension–torsion ($R_\sigma = -1$) (MPa)
σ_{D0}^{to}	fatigue limit under repeated torsion ($R_\sigma = 0$) (MPa)
σ_{D0}^{te}	fatigue limit under repeated tension ($R_\sigma = 0$) (MPa)
σ_{D0}^{te-to}	fatigue limit under repeated tension–torsion ($R_\sigma = 0$) (MPa)
$\sigma_{eq\nabla M}$	DSG equivalent stress at point M (MPa)
$\sigma_{Cr,Max}$	maximum Crossland equivalent stress on the defect surface (MPa)
$\sigma_{Cr,\infty}$	Crossland equivalent stress at infinity fare from the defect (MPa)
$\sqrt{Area}$	defect size parameter defined as the square root of the projected defect area on a plane perpendicular to the direction of the maximal principal stress (μm)
$\sqrt{Area}_{ref}$	reference defect size (μm)

In studies of A356-T6 containing observable defects [3,8,9], it was clearly shown that one of the most fatigue-life limiting defects are near-surface pores. The defect size has been shown to have a significant effect on the fatigue limit when a critical size is reached [3,8]. Whereas, the fatigue behaviour is improved when the SDAS is refined for defect free material submitted to fully reversed cyclic loadings [7,9]. Experimental investigations carried out in [10,11] have permitted both qualitative and quantitative observations of the influence of the SDAS and pore size on the fatigue life on A356-T6. Koutiri [12,13] has shown that, for cast aluminum alloy Al7Si05Cu03Mg, the mean stress has a detrimental effect that can be described by the Goodman approach.

In order to determine the critical flaw size which limits fatigue resilience, Kitigawa relationships are often used. Four principal approaches are usually employed in the literature to provide a phenomenological basis: the Murakami relationships [14], the Critical Distance Method (CDM) [15], Linear Elastic Fracture Mechanics based approaches and the Defect Stress Gradient criterion (DSG) [16,17]. A comparative study conducted by Roy et al. [7] of all four approaches for A356-T6 demonstrated that the DSG and the CDM approaches, most closely matched experimental data from multiaxial, fully reversed fatigue testing. Both of these approaches permit accounting for defect size and stress ratio effects. To the authors' knowledge, all studies seeking to link fatigue resilience to microstructural features present in A356-T6 have employed fully reversed loading. There is a paucity of fatigue data available on this alloy that includes the effect of mean stress. This key factor cannot be ignored as demonstrated for other nominally defective materials [17,18].

In this work, the effects of the mean stress, defects and microstructure (SDAS) on High Cycle Fatigue (HCF) behaviour of cast A356-T6 will be presented. Kitagawa diagrams and Haigh diagrams have been populated with the results of tension, torsion and combined tension–torsion cyclic testing for both fully reversed (load ratio $R_\sigma = -1$) and repeated (load ratio $R_\sigma = 0$) loadings. These results will be analysed and used to characterise the effects of defects in A356-T6 on the HCF behaviour. The surface response method will be used to obtain qualitative and quantitative correlation of microstructural parameters (SDAS and defect size). Finally, this analysis will be used to propose an approach to improve the DSG criterion by taking into account the SDAS effect and its correlation with defect size.

2. Experimental investigation

2.1. Material and specimens

The A356-T6 test specimens used in this investigation were sourced from material supplied by a North American automotive wheel manufacturer. The nominal chemical composition of this material is given in Table 1. Before fatigue testing, all the specimens were heat-treated to a T6 condition using the following procedure: (i) solutionized at 540 °C for 4 h and (ii) quenched in water at 60 °C and finally artificially aged at 150 °C for 3 h. The main mechanical properties for this material for fine microstructure (SDAS = 36 μm) are: Young's modulus E = 66GPa, Yield stress $R_{p0.2\%}$ = 164 MPa, tensile strength R_m = 317 MPa and elongation to failure A = 16%.

Six specimens were extracted from a low pressure die cast automotive wheel, which was casted using standard industrial condition that achieved relatively high cooling rates. These specimens represent the minimum area percent porosity (0.06%) with a fine microstructure (SDAS ~36 μm). These samples will be considered, in the present work, to be defect-free material. All other specimens were extracted from a wedge casting, shown in Fig. 1, where the casting geometry caused the cooling rates to vary according to the height in the wedge. In this casting, significant microstructural differences and defect sizes were observed based on the cooling rate and the location in height (bottom vs top in Fig. 1a). At the wedge base, where the cooling rate was high, a fine SDAS (~39–42 μm) was obtained with a low number of defects. At the top of the wedge, a coarser microstructure (~62–72 μm) and bigger

Table 1
Chemical composition of aluminum, A356.

Elements	Si	Mg	Fe	Zn	Na	Sr	Al
Wt%	6.5–7.5	0.25–0.4	0.2	0.1	0.002	0.005	91.8–93

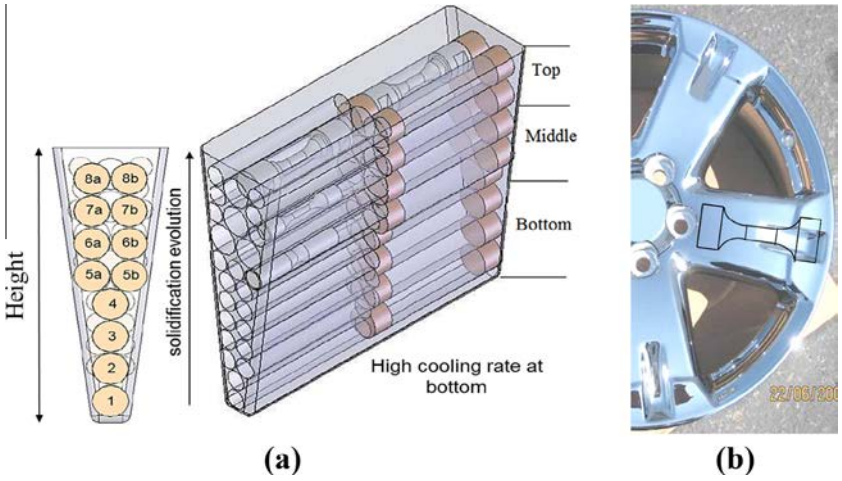

Fig. 1. Location of fatigue specimens: (a) extracted from a wedge casting, and (b) extracted from the spoke.

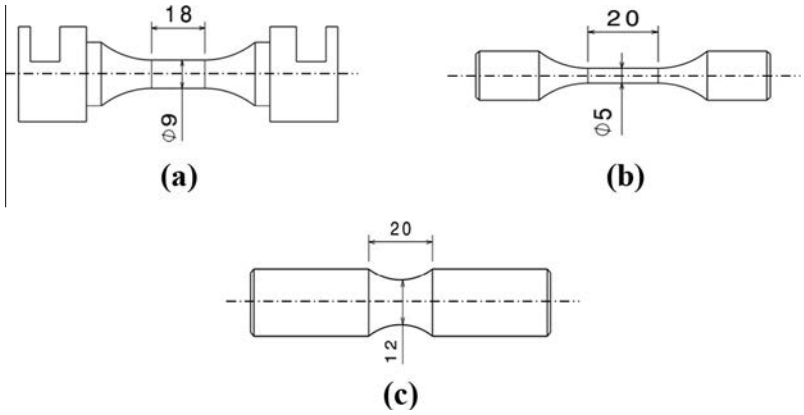

Fig. 2. Fatigue specimen geometry: (a) combined tension–torsion, (b) tensile, and (c) torsion.

defects was obtained. A variety of test specimens, with the geometries shown in Fig. 2, were extracted from the sample materials.

The microstructure of the A356-T6, shown in Fig. 3, is typical of a hypoeutectic Al–Si–Mg alloy, with primarily of aluminum dendrites (α-Al), surrounded by an Al–Si eutectic distributed around the dendrites. The SDAS were measured by using SEM micrographs with an accurate scale bar. A line parallel to the primary growth direction has been drawn and the SDAS were measured by averaging the distance between adjacent side branches on the longitudinal section of a primary dendrite as shown in Fig. 3 [5,19,20].

The grain size was also quantified using electrolytic etching with chemical reagent (66% HNO_3, 33% HCl, 1% HF) then anodizing for 5 s at 5 V and imaging quantification. The grain size quantified in Table 2 corresponds to the grains that are the most represented in the surface analysed. This parameter corresponds roughly to the maximum of the grain size distribution. It has been observed that there is a large range of grain size (200 μm–2 mm). It was observed in the wedge casting that there is no correlation between grain size distributions and cooling rate. In this context, Ceschini [21] has found a weak correlation between the distribution of the grain size and the cooling rate on the A356-T6 aluminum alloy. The grain size and SDAS variation according to the position of test specimens in the wedge casting and wheel were presented in Table 2. The variation of the cooling rate in the wedge casting with the height is the main parameter that affect the SDAS and defect sizes.

2.2. Fatigue tests

High cycle fatigue tests were carried out under tension, torsion and in phase combined tension–torsion loadings with $\sigma = \tau$. All specimens were tested at room temperature at the load ratios $R_\sigma = -1$ and $R_\sigma = 0$. All the fatigue tests were carried out under force-control machine. The fatigue tests under pure tension and pure torsion were carried out with an Amslor-Mesomart fatigue machine with frequencies of 80 Hz and 45 Hz, respectively, while the combined tension–torsion where performed on an Instron servo-Hydraulic test machine at 10 Hz. For frequency varying from 10 to 100 Hz, aluminum alloy are not found to be affected by frequency.

2.3. Determination of the fatigue limits

The step by step method [22] has been used to determine the 10^6 cycle endurance limit (heretofore referred to as the fatigue limit). The use of this method has not been found to influence the fatigue limit of this material [6]. For each specimen subjected to cyclic loading at a given stress level, the determination of the fatigue limit is carried out with the following procedure:

(i) For the case when the specimen had a direct failure before reaching 10^6 cycles during the first applied load level, the fatigue limit has been determined using the Basquin law (1):

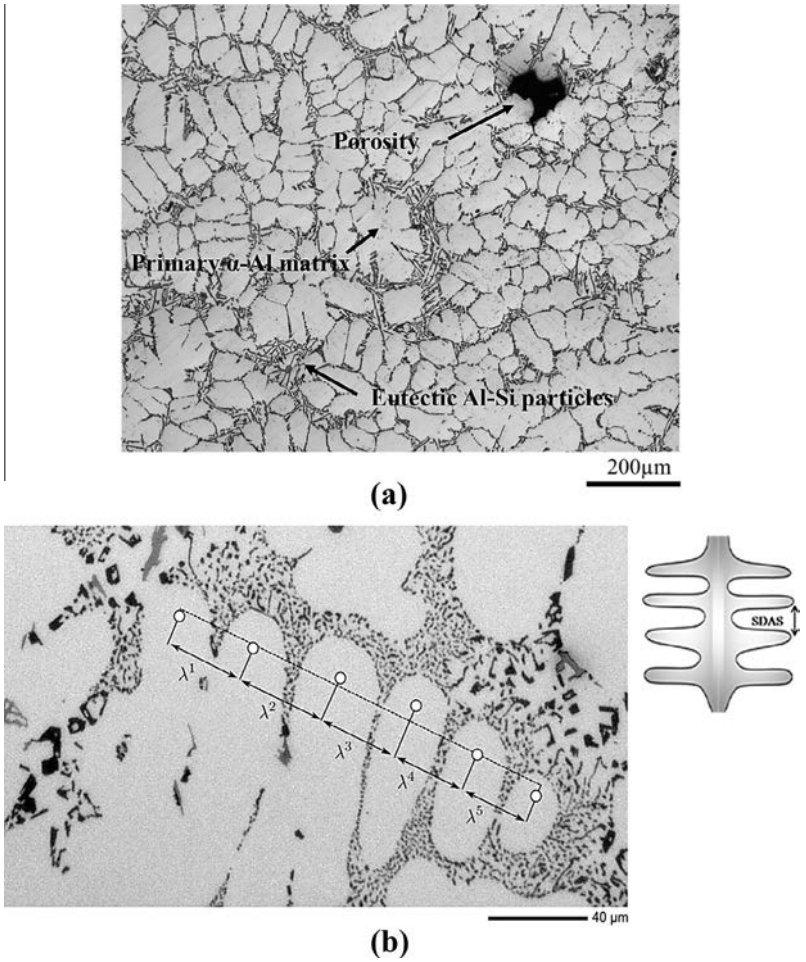

Fig. 3. (a) microstructure of A356-T6, and (b) measurement technique of the SDAS.

$$N = A\sigma_a^n \quad (1)$$

where A is a proportionality constant identified from the experimental result and n is the Basquin coefficient determined from the average results reported in previous studies [7,23–26]. The Basquin coefficient for A356-T6 has been taken to be equal to −0.15.

(ii) For specimens with several steps before failure, the fatigue limit is corrected to account for previous loading steps. Specimens that withstood 10^6 cycles at a given amplitude were loaded successively with $\Delta\sigma_a$ = 10 MPa steps until failure. The fatigue limit was then calculated via Eq. (2) [27]:

$$\sigma_D = \frac{N_f}{10^6} \times (\sigma_n - \sigma_{n-1}) + \sigma_{n-1} \quad (2)$$

where σ_D is the fatigue limit, σ_n and σ_{n-1} are the amplitude loads that caused failure and before failure and N_f is the number of cycles at the current load step to failure.

Table 2
Secondary dendrite arm spacing and grain size measurements for all used material.

Family	Height (mm)	SDAS (μm)	Grain size (μm)
Wheel	N/A	36.7 ± 8	2033 ± 50
Wedge bottom	28	39.5 ± 7.6	1655 ± 38
	58	39.7 ± 9.1	1148 ± 72
	88	47.6 ± 14.1	1051 ± 39
Wedge middle	118	57.2 ± 17.9	966 ± 41
	144	58.5 ± 21	861 ± 19
	174	59.7 ± 21.2	943 ± 51
Wedge top	204	62.6 ± 21.6	379 ± 45
	234	72.2 ± 28.2	188 ± 50

2.4. Defect characterisation

The most common nucleation sites inducing failure were at pores. SEM observations have been used to identify and to characterise the defect initiation sites on the fractured surfaces. Fig. 4 provides an example of initiation site with natural and artificial defect and for defect free material under different loading cases. The following steps were employed: (i) distinguishing between fatigue propagation and ductile failure zones, (ii) observation of radial propagation lines converging to the crack initiation site, and (iii) finally identification of the principal defect that induce the crack initiation.

Defect sizes were characterised by the $\sqrt{Area}$ parameter proposed by Murakami [14]. It is defined as the square root of the projected area of the defect on the plane perpendicular to the direction of the maximal principal stress. There are two different approaches when employing this parameter: (i) for internal defects (located at a distance greater than $\sqrt{Area}$ from the surface), the size is estimated by projecting a best-fit circle or ellipse on the defect to calculate the size; and (ii) for near-surface defects (located at a distance less than $\sqrt{Area}$ from the surface), interpolated ligaments are added up to the free surface to calculate the $\sqrt{Area}$ parameter. For cases where there were several defects in the initiation area, two approaches were taken: if the distance between two defects

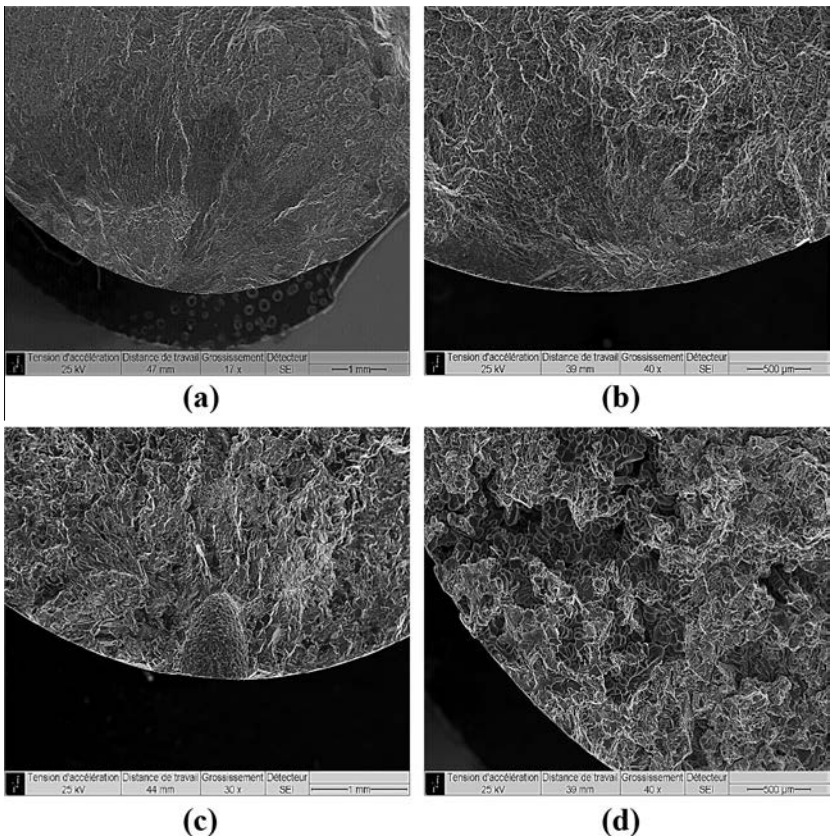

Fig. 4. SEM observation of initiation site (a) under tensile loading for defect free material at $R_\sigma = 0$, (b) under torsion loading for defect free material at $R_\sigma = 0$, (c) under combined tension–torsion loading at $R_\sigma = 0$ with artificial defect, and (d) under tensile loading at $R_\sigma = -1$ with porosity.

was larger than the biggest diameter ($D > D_{max}$), the largest defect was employed to define the $\sqrt{Area}$ parameter. Otherwise, for defects that were close ($D < D_{max}$), interpolated ligaments between defects were added to generate a regular shape to define the $\sqrt{Area}$ parameter. This method has been used on the cast AS7G06-T6 aluminum alloy which is close to the cast A356-T6 in this case of study [28].

3. Results and discussion

Analysis and discussions will be presented based on comparisons between the results from the tension, torsion and combined tension–torsion fatigue tests. For each loading case, testing was carried out with two load ratios $R_\sigma = 0$ and $R_\sigma = -1$ to characterise the effect of the mean stress on the high cycle fatigue of A356-T6. These experimental results have been used to generate Kitagawa diagrams to demonstrate the effects of both the defect size and SDAS on the fatigue limit. All the fractured surfaces were observed in order to analyse the initiation area and locate the defect size causing failure. To complete the Kitagawa diagrams, artificial defects were introduced by electro discharge machining. It is worth noticing that it has been verified in previous work of Roy [8] on the cast A356-T6 aluminum that natural and artificial defects lead to have the same influence on fatigue limit at fixed size. The results were further analysed using a response surface technique to provide a qualitative interaction between defect size and SDAS. The response surface method is used to explore relationships between dependent or independent parameters. For each experimental result, the fatigue limit with the corresponding defect size and SDAS are implemented to plot the response surfaces. In this method, the fatigue limit was considered as the response and will be presented graphically in a contour plot in terms of SDAS and defect size employing a second-degree polynomial defined as:

$$\sigma_D = X \times SDAS^2 + Y \times \sqrt{area}^2 + Z \times SDAS \times \sqrt{area} + \psi \quad (3)$$

where X, Y and Z are the coefficients of the polynomial used to fit the experimental results in the response surface method and ψ is the error.

This response surface technique using Eq. (3) provides a means to determine the impact of each parameter on the fatigue limit. The software package Minitab design of experiments is used to generate contours for the different loading cases. These experimental plans corresponds to a particular height of the response surface which efficiently describes the effect of each parameter as the defect size and the SDAS.

3.1. Tensile fatigue behaviour

For tensile loading, all of the crack initiation defects were located on fracture surfaces perpendicular to the direction of the maximum principal stress. The Kitagawa diagrams under tension are plotted in Fig. 5. It can be clearly seen that for the $R_\sigma = -1$ load ratio, there are two zones: (i) A first plateau zone where defect sizes have no effect on the fatigue limit which remains practically unchanged despite the presence of defect up to 500 μm. This defect size (500 μm) has been defined as the reference defect size by $\sqrt{Area}_{ref}$ because most of the Kitagawa diagrams given in the literature are obtained under tension for $R_\sigma = -1$. (ii) A second zone where the defect size is greater than $\sqrt{Area}_{ref}$ and there is a significant decrease in fatigue limit when the defect size increases. The

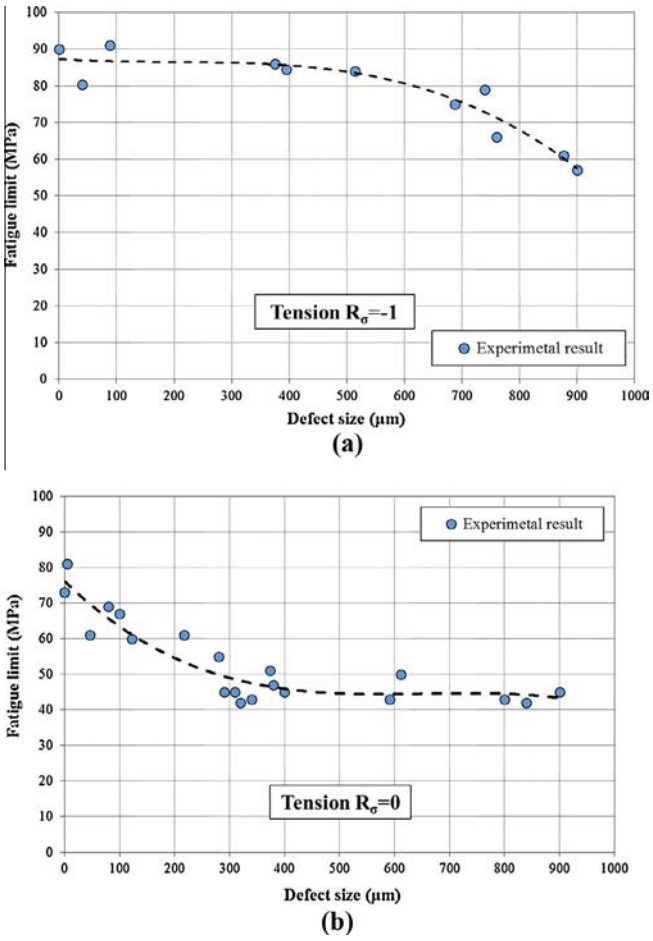

Fig. 5. Kitagawa diagram for A356-T6 with natural and artificial defects under tensile loading for load ratios of (a) $R_\sigma = 0$, and (b) $R_\sigma = -1$.

reference defect size corresponds at 10% on the reduction on the fatigue limit for defect free material.

For the $R_\sigma = 0$ load ratio results, it is clearly seen that the fatigue limit is sensitive to even small defects. The difference between the fatigue limit of defect free material and that with large defects (=800 µm) is from $\sigma^{te}_{D0} = 75$ MPa to $\sigma^{te}_{D0} = 40$ MPa for the case of $R_\sigma = 0$, however, for $R_\sigma = -1$ this difference is from $\sigma^{te}_{D-1} = 90$ MPa to $\sigma^{te}_{D-1} = 70$ MPa. We observe clearly that the reduction of the fatigue limit for large defects is more pronounced for $R_\sigma = 0$. This result illustrates the effect of tensile mean stress on the fatigue limit of defective material. It is observed that, despite the variation of SDAS between the tested specimens, there is a low scatter in the fatigue limit. This leads us to suppose that, in the case on tensile loading, the microstructure has a small effect under tension. At this stage, the effect of mean stress, seems to be more linked to the defect size than the microstructure, although changing for tested specimens as noted above.

The Haigh diagrams for this loading scenario are plotted in order to analyse the effect of mean stress on the fatigue behaviour of the defective A365 T6 submitted to cyclic tensile loading presented in Fig. 6(a). For defect free material, we observe that the stress amplitude decreases linearly as the mean stress increases. It was found a good correlation between the experimental points and the Goodman straight line for defect-free material. The according Goodman's equation is given by:

$$\sigma = \sigma^{te}_{D-1}\left(1 - \frac{\sigma_{mean}}{R_m}\right) \tag{4}$$

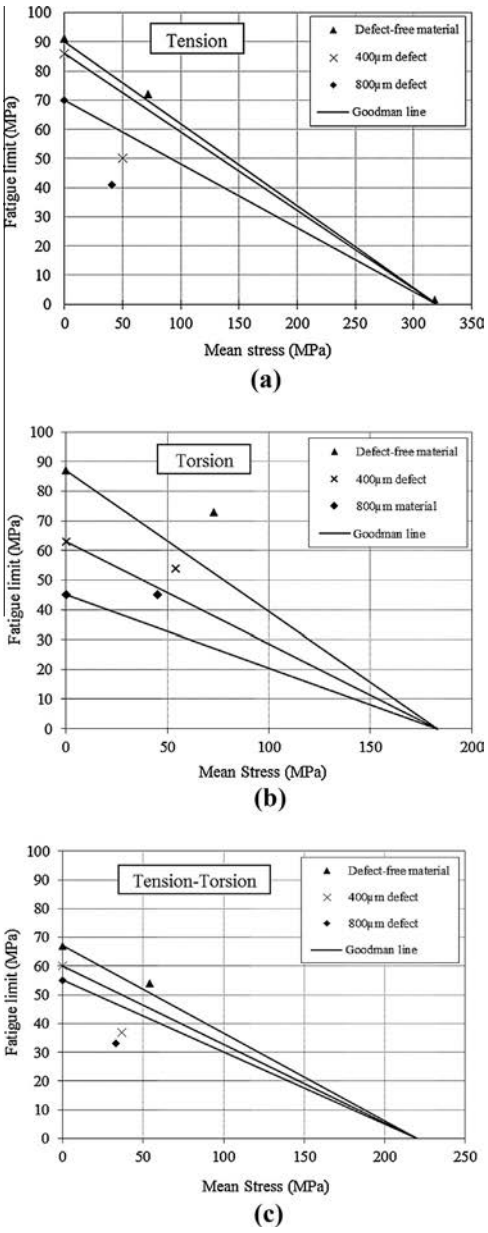

Fig. 6. Haigh diagrams for A356-T6 with experimental data extracted from Kitagawa curves under (a) tensile, (b) torsion, and (c) combined tension–torsion loading.

For the defective material, it is observed that the experimental points are below the Goodman behaviour as show in Fig. 6. It is observed that for the two loading ratios, the fatigue limit is significantly lower for defective material than the case of free defect material. Furthermore, the rate at which the fatigue limit decreases is more significant for the defective material. From these results, it appears that the fatigue limit of A356 under tensile loading conditions is very sensitive to the mean stress in presence of defects.

Fig. 7 presents the influence of the defect size and the SDAS on the fatigue limit under tensile loading conditions. For the $R_\sigma = 0$ case, a significant interaction was observed where the values of defect sizes and SDAS are relatively low. However, for large defects and low values of SDAS, the effect of the SDAS is practically insignificant. Furthermore, a slight correlation exists between the two parameters at large SDAS. For the $R_\sigma = -1$ case, a significant correlation was observed in the area where defect sizes are larger and the SDAS is relatively low. However, for small defect sizes, the

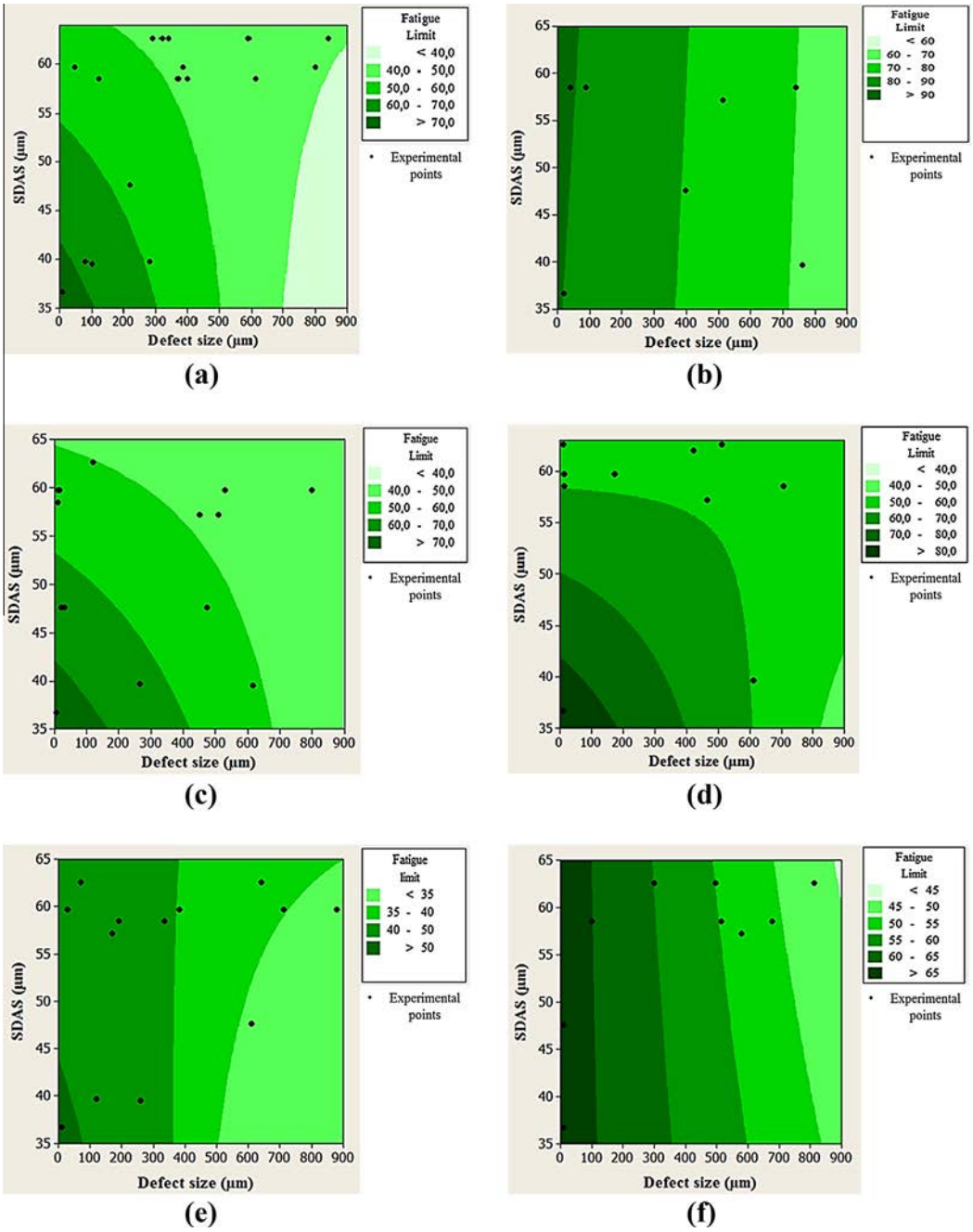

Fig. 7. Evolution of fatigue limit as a function of SDAS and defect size. The colors present the interpolation of results through the response surface method: (a) tensile loading with $R_\sigma = 0$, (b) tensile loading with $R_\sigma = -1$, (c) torsion loading with $R_\sigma = 0$, (d) torsion loading with $R_\sigma = -1$, (e) tension–torsion loading with $R_\sigma = 0$, and (f) tension–torsion for $R_\sigma = -1$.

effect of SDAS seems to be practically insignificant. These results show that for bigger defect sizes, the mean tensile stress effect is more important. For a load ratio of $R_\sigma = 0$, the interaction between the two parameters is more significant and the SDAS effect seems to be more dominant but this is lost in with the presence of a large defect.

3.2. Torsion fatigue behaviour

For torsion loading, the corresponding experimental Kitagawa diagrams are given in Fig. 8 for load ratios of $R_\sigma = 0$ and $R_\sigma = -1$. Difficulties in identifying the initiating defect were encountered for this loading case. As a result, the experimental points that were unsuccessfully classified by fractography were plotted below 100 µm in the Kitagawa analysis. Furthermore, variability in the fatigue limits were observed for material with defects smaller than 100 µm, from $\sigma_{D0}^{to} = 40$ MPa to $\sigma_{D0}^{to} = 73$ MPa for the $R_\sigma = 0$ case and from $\sigma_{D-1}^{to} = 50$ MPa to $\sigma_{D-1}^{to} = 87$ MPa for the $R_\sigma = -1$ case. It is surmised that this is due to variations in SDAS in defect-free samples extracted from different levels in the wedge casting. To highlight the effect of microstructure for those samples, the variation of fatigue limit plotted versus SDAS is presented in Fig. 9 This result demonstrates that, for both $R_\sigma = 0$ and $R_\sigma = -1$, the fatigue limit decreases significantly with the increase of SDAS in the case of defect free material.

From specimens with identifiable defects, the Kitagawa diagram (Fig. 8) shows clearly that for both of the $R_\sigma = 0$ and $R_\sigma = -1$ cases, the fatigue limit is sensitive to the defect size. The

difference between the fatigue limit of defect free material and that with the largest defect is about 50% at $R_\sigma = -1$ (from $\sigma^{to}_{D-1} = 90$ MPa to $\sigma^{to}_{D-1} = 45$ MPa) and about 37% at $R_\sigma = 0$ (from $\sigma^{to}_{D0} = 72$ MPa to $\sigma^{to}_{D0} = 45$ MPa). These results suggest that A356 is more sensitive to the presence of defects under fully reversed torsional loading as opposed to a loading scenario with a mean shear stress. As both diagrams ($R_\sigma = 0$ and $R_\sigma = -1$) converge to the same fatigue limit, it appears that there is no significant effect of mean stress under torsion loading for material with large defects. Contrary to the tension load, under torsion, it was difficult to identify a reference defect size for both loading cases.

In order to examine the interaction between the defect size and the SDAS on the fatigue limit obtained from torsion tests, the response surfaces have been plotted in Fig. 7. For both loading ratios, a significant correlation was observed where defect sizes are relatively small. This interaction between parameters continues until large defects are realized (~600 μm). The effect of SDAS is more significant for small defect sizes, explaining the variation seen in Kitagawa analysis. As the size of the defect increases, the effect of the SDAS decreases until it is practically insignificant for large defects. Overall, the interaction between SDAS and defect size is more significant for torsion compared to tensile loading conditions, and that the SDAS effect is important.

To highlight the effect of mean stress, Goodman lines have been plotted on a Haigh diagram in Fig. 6(b) corresponding to defective and none defective material under torsion loading. Here, a departure from what was seen under tensile conditions is observed: (i) the mean shear stress has a small influence for defect-free material and (ii) this effect decreases in the presence of defects. For a defect size of 800 μm, the mean stress has no effect and the fatigue limit remains practically unchanged. This result demonstrates that the effect of mean shear stress on the fatigue of A356-T6 is less important as the defect size increases. Clearly, the effect of cyclic shear

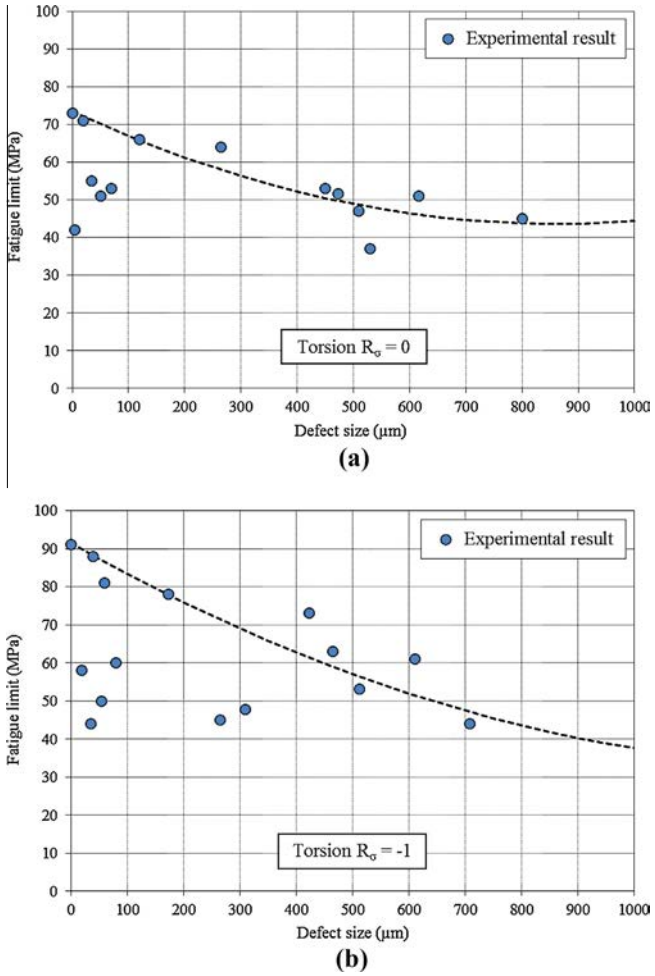

Fig. 8. Kitagawa diagrams for A356-T6 with natural and artificial defects under torsion loading for load ratios of (a) $R_\sigma = 0$, and (b) $R_\sigma = -1$.

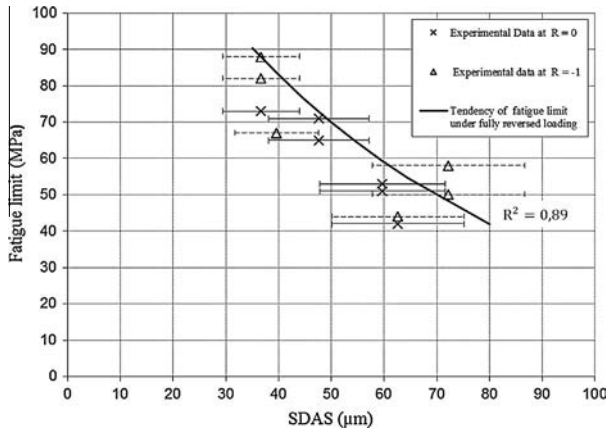

Fig. 9. Fatigue limit variation under torsion loading for defect-free specimen for load ratios of $R_\sigma = 0$ and $R_\sigma = -1$ as a function of SDAS.

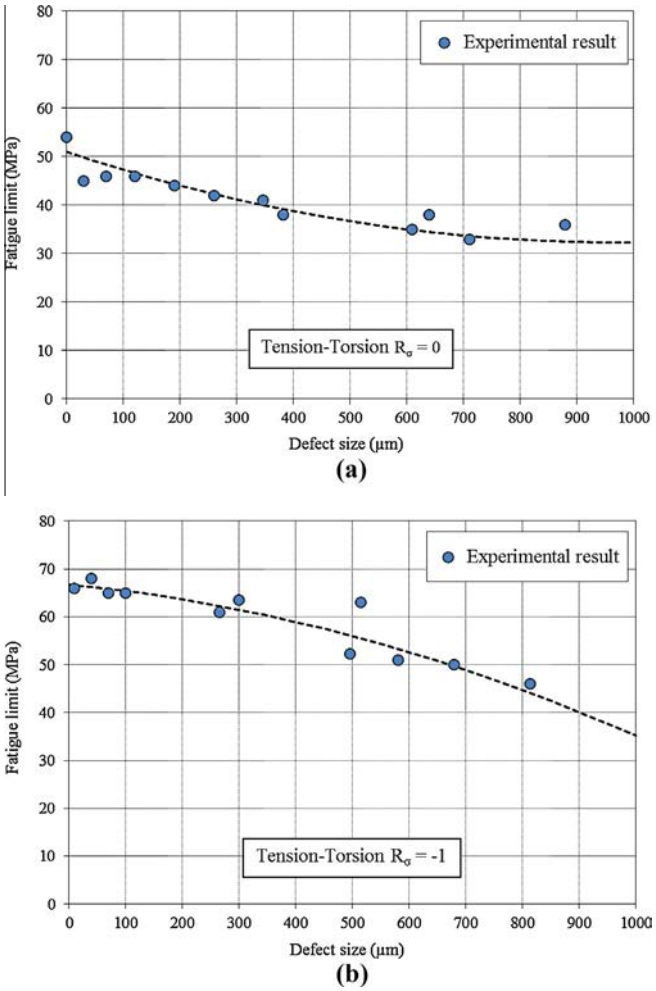

Fig. 10. Kitagawa diagram for A356-T6 with natural and artificial defects under combined tension–torsion loading for load ratios of (a) $R_\sigma = 0$, and (b) $R_\sigma = -1$.

stress is dependent on microstructure rather than the mechanical effects linked to defect size.

3.3. Tension–torsion fatigue behaviour

The fracture surfaces of specimens tested under combined tension–torsion loading were found to be perpendicular to the direction of the maximum principal stress, similar to that seen under tensile fatigue loading. The corresponding experimental Kitagawa diagrams for tension–torsion tests are plotted in Fig. 10 for both of the load ratios $R_\sigma = 0$ and $R_\sigma = -1$. From these diagrams, a first plateau zone can be obtained where defect sizes have a slight effect on the fatigue limit. Then a reference defect size $\sqrt{Area}_{ref} = 500$ μm can be defined. For defective material, a slight reduction in the fatigue limit is observed. This effect is relatively insignificant between small and large defects size (800 μm) unlike what was observed for the pure tensile and torsion loading cases (from $\sigma_{D0}^{te-to} = 45$ MPa to $\sigma_{D0}^{te-to} = 35$ MPa for $R_\sigma = 0$ and from $\sigma_{D-1}^{te-to} = 68$ MPa to $\sigma_{D-1}^{te-to} = 45$ MPa for $R_\sigma = -1$).

Table 3
Experimental data and identified parameters of the improved DSG criterion.

Experimental data		Identified parameters	
$\sigma_{D-1}^{to}(\lambda_2 = 36.7\ \mu m)$	88	β_0 (MPa)	167
$\sigma_{D-1}^{to}(\lambda_2 = 72.2\ \mu m)$	50	α_0	1.8
$\sigma_{D0}^{ta}(\lambda_2 = 36.7\ \mu m)$	73	λ_0 (μm)	60
$\sigma_{D-1}^{ta}(\sqrt{aire} = 688\ \mu m)$	75	a_∇ (μm)	470

The response surface analysis was conducted for combined tension–torsion loading results and the fatigue limit for the load ratios of $R_\sigma = 0$ and $R_\sigma = -1$ are plotted versus SDAS and defect size in Fig. 7. For both $R_\sigma = 0$ and $R_\sigma = -1$, it is observed that the effect of defect size is more significant than the effect of the SDAS. In comparing the relationships between the two load ratios, the interaction between SDAS and defect size is more significant for $R_\sigma = 0$ as compared to $R_\sigma = -1$.

In the Haigh diagram for the tension–torsion results, shown in Fig. 6(c), it is observed that the experimental results of defect-free adhere to Goodman line. In the presence of defects, the experimental results become more sensitive to the mean stress resulting in a decrease in the fatigue limit and a departure from the Goodman relationship.

It is therefore posited that A356-T6 is sensitive to the mean stress and the fatigue limit decreases linearly for defect-free material. In presence of defects, the effect of mean stress becomes more apparent and cannot be ignored.

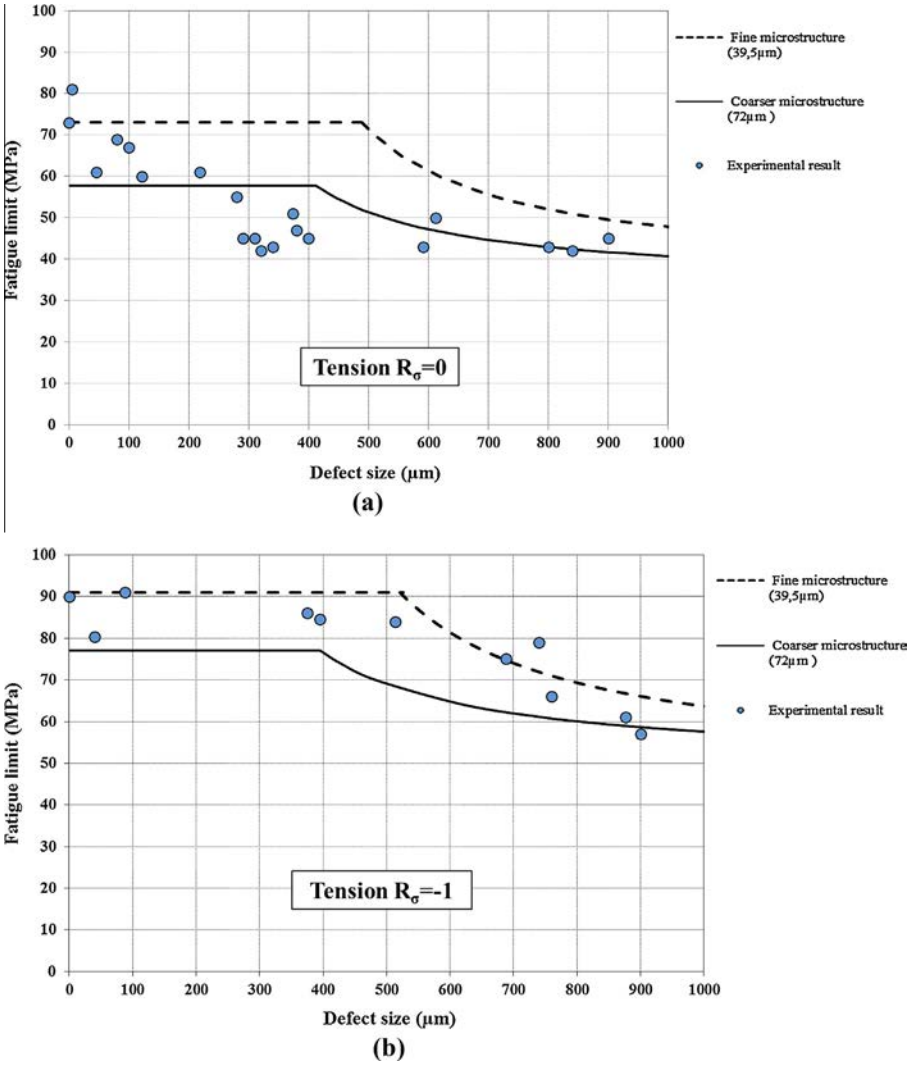

Fig. 11. Predicted Kitagawa diagram using modified DSG criterion for tensile loading with load ratios of (a) $R_\sigma = 0$, and (b) $R_\sigma = -1$.

4. Modelling Kitagawa diagram under multiaxial loading

4.1. Improvement of the defect stress gradient criterion

The Defect Stress Gradient (DSG) criterion established by Nadot et al. [16] and generalized by Vincent [29] describes the influence of a defect on the fatigue limit theory. In this study, we adopt to use the Crossland criterion to calculate the fatigue equivalent stress in the DSG criterion. The DSG criterion is given by Eq. (5).

$$\sigma_{eq\nabla M} = \sigma_{Cr,Max} - a_{\nabla}\frac{\sigma_{Cr,Max} - \sigma_{Cr,\infty}}{\sqrt{area}} \leqslant \beta_{cr} \tag{5}$$

The DSG criterion takes into account both the defect size and the mean stress effects on the fatigue limit. However, the DSG criterion does not account the microstructural variation, which the current experimental results have shown to have an effect on A356-T6 alloy. The DSG criterion has therefore been extended to account for SDAS variations. Pivotal to the DSG criterion is an accurate fatigue limit under torsion loading (σ^{to}_{D-1}). As the previously presented experimental results clearly show, the torsion fatigue limit for free defect material is correlated with the SDAS for both $R_\sigma = 0$ and $R_\sigma = -1$. As the β_{cr} parameter in the DSG criterion is dependent on the fully reversed torsion fatigue limit σ^{to}_{D-1}, the β_{cr} parameter may be replaced by a function that is SDAS-dependent. After Maijer et al. [30], an empirical relationship between the yield stress and the SDAS (λ_2) for A356-T6 can be expressed as:

$$\sigma_y = \sigma_0 \exp\left(-\frac{\lambda_2}{\lambda_0}\right) \tag{6}$$

where the empirical constant $\sigma_0 = 278$ MPa, and $\lambda_0 = 244$ μm.

We consider as a working hypothesis that the β_{cr} parameter changes with SDAS parameter (λ_2) by an exponential function with the same form of Eq. (6). Following this hypothesis, the material parameter β_{cr} of the gradient criterion can be related to λ_2 by Eq. (7). Fig. 9, demonstrates that this empirical function (7) fits well the fatigue limit for defect-free material describing the variation of σ^{to}_{D-1} based on SDAS.

$$\beta_{cr}(\lambda_2) = \beta_0 \exp\left(-\frac{\lambda_2}{\lambda_0}\right) \tag{7}$$

where $\beta_0 = 164$ MPa, and $\lambda_0 = 58.5$ μm identified experimentally.

Substituting Eq. (7) into the standard DSG criterion given in Eq. (5), the following expression is obtained:

$$\sigma_{eq\nabla M} = \sigma_{Cr,Max} - a_{\nabla}\frac{\sigma_{Cr,Max} - \sigma_{Cr,\infty}}{\sqrt{area}} \leqslant \beta_0 \exp\left(-\frac{\lambda_2}{\lambda_0}\right) \tag{8}$$

with

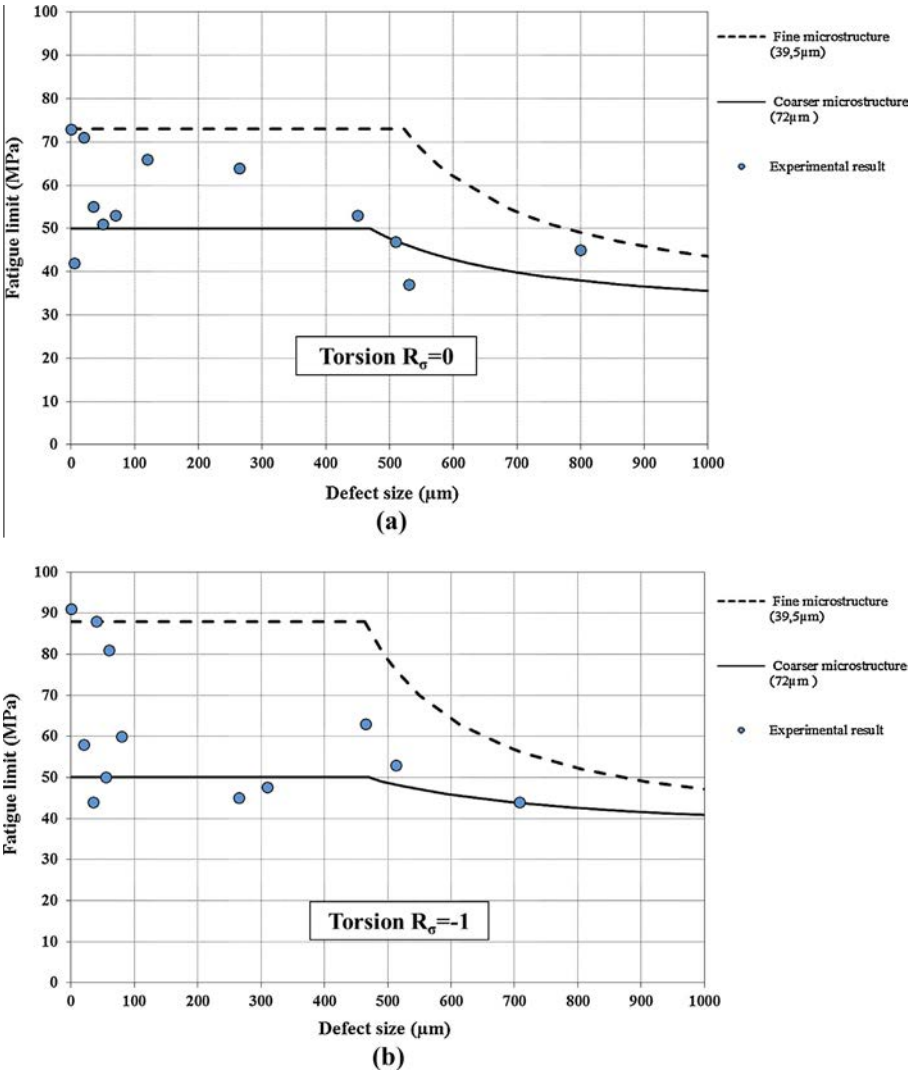

Fig. 12. Predicted Kitagawa diagram using modified DSG criterion for torsion loading with load ratios of (a) $R_\sigma = 0$, and (b) $R_\sigma = -1$.

$$\sigma_{Cr} = \sqrt{J_{2,a}} + \alpha_{cr} J_{1,max} \leqslant \beta_{cr} \tag{9}$$

4.2. Parameter identification for the improved DSG criterion

The experimental results have shown that the β_{cr} which corresponds to the fully reversed torsion fatigue limit σ_{D-1}^{to}, is correlated with the SDAS. As α_{cr} is a function of the β_{cr} parameter according to the Eq. (10), an expression similar to that used for β_{cr} has been adopted for α_{cr} given by the Eq. (11). The Eq. (10) is coming from the Crossland criteria for a fully reversed tension fatigue limit.

$$\alpha_{cr}(\lambda_2) = \frac{\beta_{cr}(\lambda_2) - \frac{\sigma_{D-1}^{ta}}{\sqrt{3}}}{\frac{\sigma_{D-1}^{ta}}{3}} \tag{10}$$

$$\alpha_{cr}(\lambda_2) = \alpha_0 \exp\left(-\frac{\lambda_2}{\lambda_0}\right) \tag{11}$$

The identification of α_0, β_0 and λ_0 parameters are performed using the fatigue limit for fully reversed torsion results with different microstructure: $\sigma_{D-1}^{to}(\lambda_2 = 36.5) = 88$ MPa and $\sigma_{D-1}^{to}(\lambda_2 = 72\ \mu m) = 48$ MPa.

The identification of the parameter a_∇ needs the fatigue limit for a given defect. In this study, a defect size of 690 μm corresponding to a fatigue limit $\sigma_{D-1}^{ta}(\sqrt{area} = 690\ \mu m) = 75$ MPa has been used. The expression for the parameter a_∇ is determined by equalizing the two terms of the inequality in Eq. (8). Then, the DSG criterion (Eq. (4)) can be transformed into

$$a_\nabla = \frac{\sqrt{area}(\sigma_{Cr,Max} - \sigma_{Cr,\infty})}{\sigma_{Cr,Max} - \beta_{cr}(\lambda_2)} \tag{12}$$

The identification of all parameters of DSG criterion was made with four experimental results. The experimental data used for identification as well as the identified parameters are given in Table 3.

4.3. Simulation of the Kitagawa diagram

This improved DSG criterion has been employed to predict the Kitagawa diagram for multiaxial loading by accounting for both defect size and the SDAS. The simulated diagrams are generated in a piece-wise continuous manner, with two functions employed to describe behaviour in appropriate regions:

(i) The first function accounts for where defect sizes are small and the material is considered practically defect-free. Here, the fatigue limit remains stable and depends only on the SDAS. It is given by the following expression:

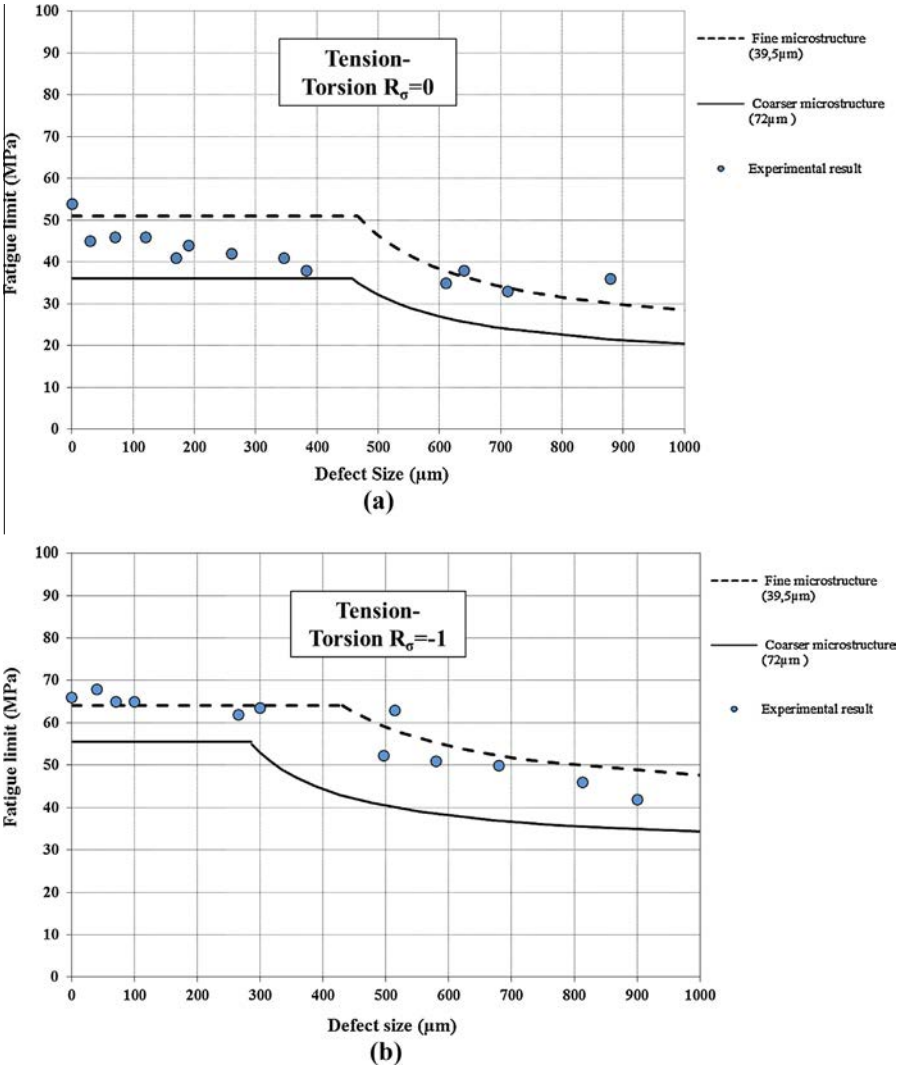

Fig. 13. Predicted Kitagawa diagram using modified DSG criterion for combined tension–torsion loading with load ratios of (a) $R_\sigma = 0$, and (b) $R_\sigma = -1$.

$$\sigma_{eq\nabla M} = \sigma_{Cr,Max} = \beta_0 \exp\left(-\frac{\lambda_2}{\lambda_0}\right) \quad (13)$$

(ii) The second function describes where the fatigue limit is strongly influenced by both defect size and SDAS as dictated by the following expression:

$$\sigma_{eq\nabla M} = \sigma_{Cr,Max} - a_{\nabla}\frac{\sigma_{Cr,Max} - \sigma_{Cr,\infty}}{\sqrt{area}} \quad (14)$$

Eq. (14) does not provide a threshold for the fatigue limit so using equation 13 we set a threshold for small defects as shown in Figs. 11–13.

4.4. Comparison between simulation and experimental results

The improved DSG criterion has been used to predict the Kitagawa diagrams for A356-T6 with fine and coarse SDAS for all the loading cases. The simulation of Kitagawa diagram corresponding to SDAS of 36.5 μm and 72 μm are plotted and compared with the experimental data in Figs. 11–13. This data was used because the SDAS values form the upper and lower bounds of the tested material. The improved DSG criterion describes adequately the experimental results quite well for all the loading cases and the predicted Kitagawa relationships are coherent with the experimental results. The diagram is constituted by two different zones: a first zone where the defect size has no influence and a second zone where the criterion describes the decrease trend of the fatigue limit versus defect size. Moreover, the improved DSG criterion has the advantage to take into account the SDAS effect in addition to the defect size.

The detailed analyses show the following observations:

(i) Fig. 11 shows the Kitagawa diagram predicted for tensile loading. For the two load ratios, it can be seen that the reference defect size which delineates that transition between the two zones depends on the microstructure. As the reference defect size is much larger for fine SDAS, it appears that there are potentially more effective short micro-crack propagation present around defects at this level of microstructural refinement. For the bigger defects, a decrease in the fatigue limit for the two SDAS is observed. The Kitagawa diagrams show that the fatigue limits for fine microstructures are greater than those obtained for larger SDAS, however this difference decreases as the defect size increases. This trend continues until the two curves converge. This leads to conclude that, even in presence of defects, the microstructure has an appreciable effect on the fatigue limit of A356-T6. For big defects size, both curve meet. This indicates that there is an important amount of plasticity at the tip of greater defects, which dominate the SDAS effect.

(ii) Considering the results for torsional loading presented in Fig. 12, the modified DSG criterion correctly describes the trend of the fatigue limit. From these diagrams, it is clear that in torsion, the microstructure characterised by SDAS parameter has a detrimental effect on the fatigue limit. Unlike what was observed under tensile, the microstructure has an important effect under torsion fatigue test even for defects smaller than the reference defect size. The impact of SDAS on the fatigue limit is more pronounced for $R_\sigma = -1$. With the modified DSG criterion for low and high SDAS, it is observed that the effect of SDAS decreases with increasing of defect size. Indeed, for large defects, both curves meet implying that the defect effect is dominant.

(iii) For the combined tension–torsion results shown in Fig. 13, similar trends to those observed for tensile conditions are evident. The reference defect size depends on the microstructure, and in presence of defects close to reference defect sizes, there is an interaction between the microstructure and defect size effect.

As a general conclusion, in all loading cases, the modified DSG criterion correctly predicts the correlation and the influence of defects and microstructure on the fatigue limit. The accuracy of the predicted Kitagawa curves were not found to favour one loading ratio versus to the other. Furthermore, it has been found that the reference defect size is affected by the microstructure.

5. Conclusions

Kitagawa diagrams have been obtained for A356-T6 submitted to six different load cases: tension, torsion and combined tension–torsion at $R_\sigma = 0$ and $R_\sigma = -1$. From this study, it may be concluded that:

(i) The plateau of Kitagawa diagram (for small defect) is strongly dependent on multiaxiality and mean stress. It is not possible on A356-T6 to derive a unique critical allowable defect size from tension for $R_\sigma = -1$.

(ii) The influence of mean stress on the fatigue limits is a function of defect size and loading. Under Torsion loading, whatever the defect size, the influence of mean stress on the fatigue limit is low as often observed on metallic materials. Under tension and combined tension–torsion loading, the effect of mean stress is much more pronounced in the presence of a defect compared to defect free material.

(iii) The influence of microstructure characterised by SDAS is a function of loading. Under torsion loading, the microstructure has a significant effect for defect-free material and governs the fatigue limit. For defective material, the interaction between the defect size and microstructure cannot be neglected. In tensile and combined tension–torsion tests, the effect of the mean stress is important and is much more appreciable in the presence of defects.

(iv) Experimental results leads to the conclusion that allowable defect size, sensitivity to mean stress and SDAS is not independent on loading type. Therefore, it is necessary to evaluate the influence of these parameters through a general multiaxial modelling. A modification to the DSG criterion has been implemented that introduces parameters to account for SDAS. The modified DSG criterion was employed to predict successfully Kitagawa relationships and examine fatigue limit trends as a function of defect size and SDAS.

Acknowledgement

This work pertains to the French Government program "Investissements d'Avenir" (LABEX INTERACTIFS, reference ANR-11-LABX-0017-01).

References

[1] Li P, Maijer DM, Lindley TC, Lee PD. A through process model of the impact of in-service loading, residual stress, and microstructure on the final fatigue life of an A356 automotive wheel. Mater Sci Eng, A 2007;460:20–30.

[2] Tokaji K. Notch fatigue behaviour in a Sb-modified permanent-mold cast A356-T6 aluminium alloy. Mater Sci Eng, A 2005;396(1):333–40.

[3] Gall K, Horstemeyer M, McDowell DL, Fan J. Finite element analysis of the stress distributions near damaged Si particle clusters in cast Al–Si alloys. Mech Mater 2000;32(5):277–301.

[4] Yi JZ, Gao YX, Lee PD, Lindley TC. Effect of Fe-content on fatigue crack initiation and propagation in a cast aluminum–silicon alloy (A356-T6). Mater Sci Eng, A 2004;386(1):396–407.

[5] Wang QG, Apelian D, Lados DA. Fatigue behavior of A356/357 aluminum cast alloys. Part II – Effect of microstructural constituents. J Light Met 2001;1(1):85–97.
[6] Roy M, Nadot Y, Maijer DM, Benoit G. Multiaxial fatigue behavior of A356-T6. Fatigue Fract Mater Struct 2012;35(12):1148–59.
[7] Gao YX, Yi JZ, Lee PD, Lindley TC. A micro-cell model of the effect of microstructure and defects on fatigue resistance in cast aluminum alloys. Acta Mater 2004;52(19):5435–49.
[8] Roy MJ, Nadot Y, Nadot-Martin C, Bardin PG, Maijer DM. Multiaxial Kitagawa analysis of A356-T6. Int J Fatigue 2011;33(6):823–32.
[9] Jeong CY, Kang CS, Cho JI, Oh IH, Kim YC. Effect of microstructure on mechanical properties for A356 casting alloy. Int J Cast Met Res 2008; 21(1–4):193–7.
[10] Bonollo F, Tovo R. Fatigue in Al casting alloys: metallurgical aspects. TALAT Lect 1999;1254:3–16.
[11] Gall K, Yang N, Horstemeyer M, McDowell DL, Fan J. The influence of modified intermetallics and Si particles on fatigue crack paths in a cast A356 alloy. Fatigue Fract Eng Mater Struct 2000;23:159–72.
[12] Koutiri I, Bellett D, Morel F, Augustins L, Adrien J. High cycle fatigue damage mechanisms in cast aluminium subject to complex loads. Int J Fatigue 2013;47:44–57.
[13] Koutiri I, Bellett D, Morel F, Pessard E. A probabilistic model for the high cycle fatigue behaviour of cast aluminium alloys subject to complex loads. Int J Fatigue 2013;47:137–47.
[14] Murakami Y. Metal fatigue: effects of small defects and nonmetallic inclusions. Elsevier Editor; 2002.
[15] Susmel L, Taylor D. The theory of critical distances to predict static strength of notched brittle components subjected to mixed-mode loading. Eng Fract Mech 2008;75(3):534–50.
[16] Nadot Y, Billaudeau T. Multiaxial fatigue limit criterion for defective materials. Eng Fract Mech 2006;73(1):112–33.
[17] Gadouini H, Nadot Y, Rebours C. Influence of mean stress on the multi-axial fatigue behaviour of defective materials. Int J Fatigue 2008;30(9): 1623–33.
[18] Marquis G, Socie D. Long-life torsion fatigue with normal mean stress. Fatigue Fract Eng Mater Struct 2000;23:293–300.
[19] Zeren Muzaffer. Effect of copper and silicon content on mechanical properties in Al–Cu–Si–Mg alloy. J Mater Process Technol 2005:292–8.
[20] Odanović Z, Durđević M, Krstić Pavlović J, Arsić M, Katavić B. Some applications of the image analysis in the metal material science. Acta Phys Polonica 2012;121.
[21] Ceschini L, Morri A, Morri A, Pivetti G. Predictive equations of the tensile properties based on alloy hardness and microstructure for an A356 gravity die cast cylinder head. Mater Des 2011;32(3):1367–75.
[22] Bellows RS, Muju S, Nicholas T. Validation of the step test method for generating Haigh diagrams for Ti–6Al–4V. Int J Fatigue 1999;21:687–97.
[23] Brochu M, Verreman Y, Ajersch F, Bouchard D. High cycle fatigue strength of permanent mold and rheocast aluminum 357 alloy. Int J Fatigue 2010;32(8):1233–42.
[24] Jana S, Mishra RS, Baumann JB, Grant G. Effect of friction stir processing on fatigue behavior of an investment cast Al–7Si–0.6 Mg alloy. Acta Mater 2010;58(3):989–1003.
[25] Wang QG, Apelian D, Lados DA. Fatigue behavior of A356-T6 aluminum cast alloys. Part I. Effect of casting defects. J Light Met 2001;1(1):73–84.
[26] Ludwig W, Buffiere JY, Savelli S, Cloetens P. Study of the interaction of a short fatigue crack with grain boundaries in a cast Al alloy using X-ray microtomography. Acta Mater 2003;51(3):585–98.
[27] Lanning DB, Nicholas T, Haritos GK. On the use of critical distance theories for the prediction of the high cycle fatigue limit stress in notched Ti–6Al–4V. Int J Fatigue 2005;27(1):45–57.
[28] Mu P, Nadot Y, Nadot-Martin C, Chabod A, Serrano-Munoz I, Verdu C. Influence of casting defects on the fatigue behavior of cast aluminum AS7G06-T6. Int J Fatigue 2014;63:97–109.
[29] Vincent M, Nadot-Martin C, Nadot Y, Dragon A. Fatigue from defect under multiaxial loading: Defect Stress Gradient (DSG) approach using ellipsoidal equivalent inclusion method. Int J Fatigue 2014;59:176–87.
[30] Maijer DM, Gao YX, Lee PD, Lindley TC, Fukui T. A through-process model of an A356 brake caliper for fatigue life prediction. Metall Mater Trans A 2004;35A.